Supporting Material

Enhanced Hydrogen Evolution Reaction *via* Photoelectrochemical Water Splitting Utilizing Asymmetric MoSSe under a Low External Magnetic Field

Krishnendu Roy, Dibyendu Ghosh, Soumyajit Maitra, and Praveen Kumar*

School of Materials Science, Indian Association for the Cultivation of Science, Kolkata-700032, India
**Email for Correspondence: praveen.kumar@iacs.res.in*

Table S1: Experimental and computational Raman modes of MoSSe.

	Computation		Experiment	
	A_{1g}	E_{2g}^{1}	A_{1g}	E_{2g}^{1}
MoSSe	283 cm^{-1}	339 cm^{-1}	284 cm^{-1}	338 cm^{-1}

Table S2: Photocurrent of different PCs at two different biases.

Photocathode	**Photocurrent density (j_p) in mA/cm² @0V vs RHE**	**Photocurrent density (j_p) in mA/cm² @1.15 V vs RHE**
SiNW	-0.2	-4.48
$MoSe_2$/SiNW	-0.45	-15.01
MoS_2/SiNW	-0.87	-17.47
MoSSe/SiNW	-2.24	-20.48
MoSSe/SiNW @0.1T	-2.98	-21.98
MoSSe/SiNW @0.2 T	-3.44	-24.73
MoSSe/SiNW @0.4 T	-4.40	-27.08
MoSSe/SiNW @0.5 T	-4.81	-27.52
Mo_2CT_x/MoSSe/SiNW	-3.69	-23.50
Mo_2CT_x/MoSSe/SiNW @0.4 T	-5.61	-32.25

Table S3: Built-in potential of different PCs from Mott-Schottky analyses.

Photocathode	**Built-in potential in V (vs RHE)**
SiNW	-0.26
$MoSe_2$/SiNW	-0.018
MoS_2/SiNW	0.15
MoSSe/SiNW	0.27
Mo_2CT_x/MoSSe/SiNW	0.40

Table S4: Comparison of onset potential and photocurrent density among different photocathodes for PEC HER.

Materials	Electrolyte	Onset potential V vs RHE	J_{photo} mA/cm^2	Year	Ref.
$Cu_2O/Ga_2O_3/TiO_2/RuO_x$	potassium phosphate solution with a pH 7 buffer solution	0.92	-8.6 @0V vs RHE	2022	1
VS_2/SiNW	Neutral electrolyte pH 7	0.874	-17 @ -0.53 V vs RHE	2022	2
$CuInS_2/CdS/MoS_2$	0.1 M Na_2SO_4	0.86	-1.75 @ 0 V vs RHE	2023	3
$Pt/TiO_2/CdS/Sb_2Se_3$ /Au/FTO	0.5 M H_2SO_4	0.5	~ -23@0 V vs RHE	2020	4
Mo_2CT_x/MoSSe/Si NW	0.5 M H_2SO_4	0.42	-3.69 @0 V vs RHE	2023	This work
Mo_2CT_x/MoSSe/Si NW @ 0.4 T magnetic field	0.5 M H_2SO_4	0.35	-5.61@0 V vs RHE	2023	This work
Si/MoS_x	0.5 M H_2SO_4	0.31	-28.2 @ 0 V vs RHE	2021	5
Si NW/$NiCo_2S_4$	0.5 M H_2SO_4	~ 0.3	-15 @ -0.8 V vs RHE	2023	6
SiNWs@MoS_2/NiS_2	0.5 M Na_2SO_4	0.3	-21.4 @ -0.9 V vs RHE	2023	7
FTO/Au/Sb_2Se_3/TiO_2/Pt	0.5 M H_2SO_4	0.3	-11.3@ 0 V vs RHE	2021	8
Si/MoS_2	0.5 M H_2SO_4	0.25	-30 @ 0V vs RHE	2021	9
$MoS_2/MoSe_2$/SiNW	0.5 M H_2SO_4	0.23	-0.9 @ 0 V vs RHE	2022	10

SiNW/Au/CoS	0.5 M H_2SO_4	0.2	-33.1 @ 0 V vs RHE	2023	11
TiS_2 QDs/WS_2/polydimethyls-iloxane	0.5 M H_2SO_4	0.038	~ -4.1 @ -0.2 V vs RHE	2023	12

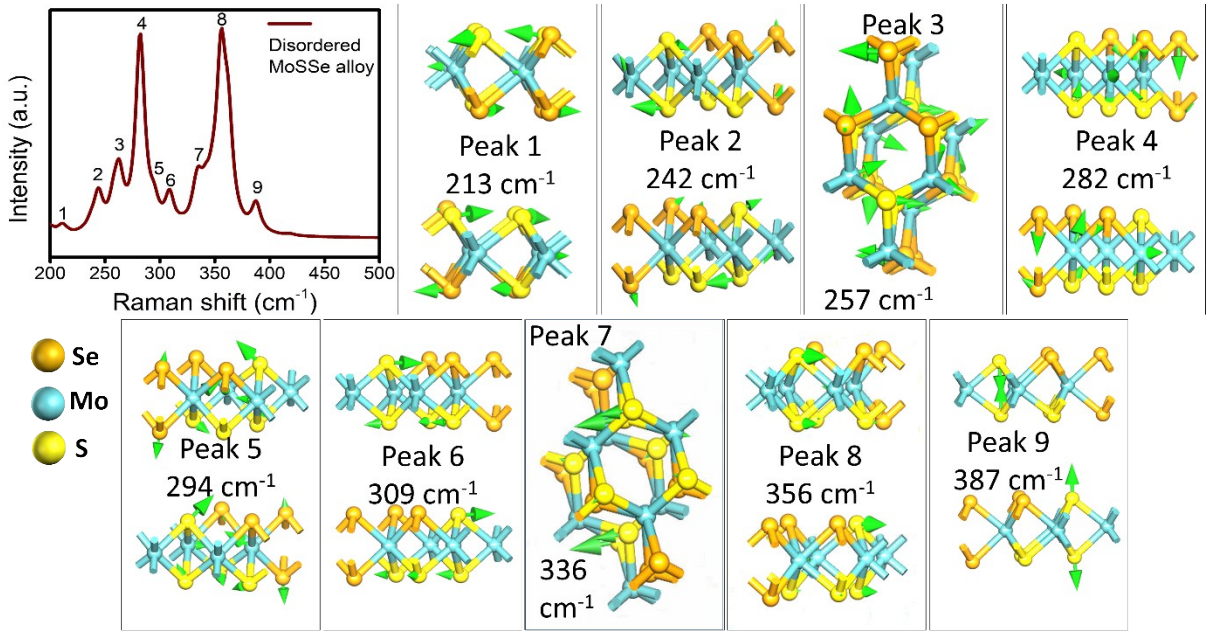

Fig. S1. Raman spectrum of randomized disordered MoSSe alloy simulated by DFT and Raman vibrational mode corresponding to every peak. The representative atomic colours of Mo, S, and Se are given.

Supporting Material Note 1: The different peaks in Fig. S1 originated due to different contributions. Peak 1 is due to an in-plane stretching characteristic of the E^1_{2g} mode of Janus MoSSe (213 cm^{-1}). Peak 2 is due to out-of-plane A_{1g}-like vibration from the $MoSe_2$ fragments and E^1_{1g} like in-plane asymmetric stretching from the MoS_2 fragments (242 cm^{-1}). In-plane E^1_{2g} mode from $MoSe_2$ fragment coupled with out-of-plane stretching of MoSSe units causes peak 3 (257 cm^{-1}). Peak 4 is caused by out-of-plane anti-symmetric bending of the Se-Mo-Se bond (282 cm^{-1}). A^1_{1g} like the out-of-plane motion of the Se atoms from the $MoSe_2$ impurity fragment coupled to the out-of-plane bending mode of the S-Mo-S fragment (294 cm^{-1}) gives rise to peak 5. Peak 6 is due to the antisymmetric in-plane bending of the S-Mo-S unit coupled with the antisymmetric in-plane E_{1g}-like stretching of MoS_2 fragments (309 cm^{-1}). Peak 7, 8, and 9 are due to the in-plane wagging motion of S atoms from the MoS_2 and MoSSe fragments

(336 cm^{-1}), in-plane E^{2}_{2g} vibrational mode of Janus MoSSe (356 cm^{-1}) and out-of-plane MoS_2 vibration (387 cm^{-1}), respectively.

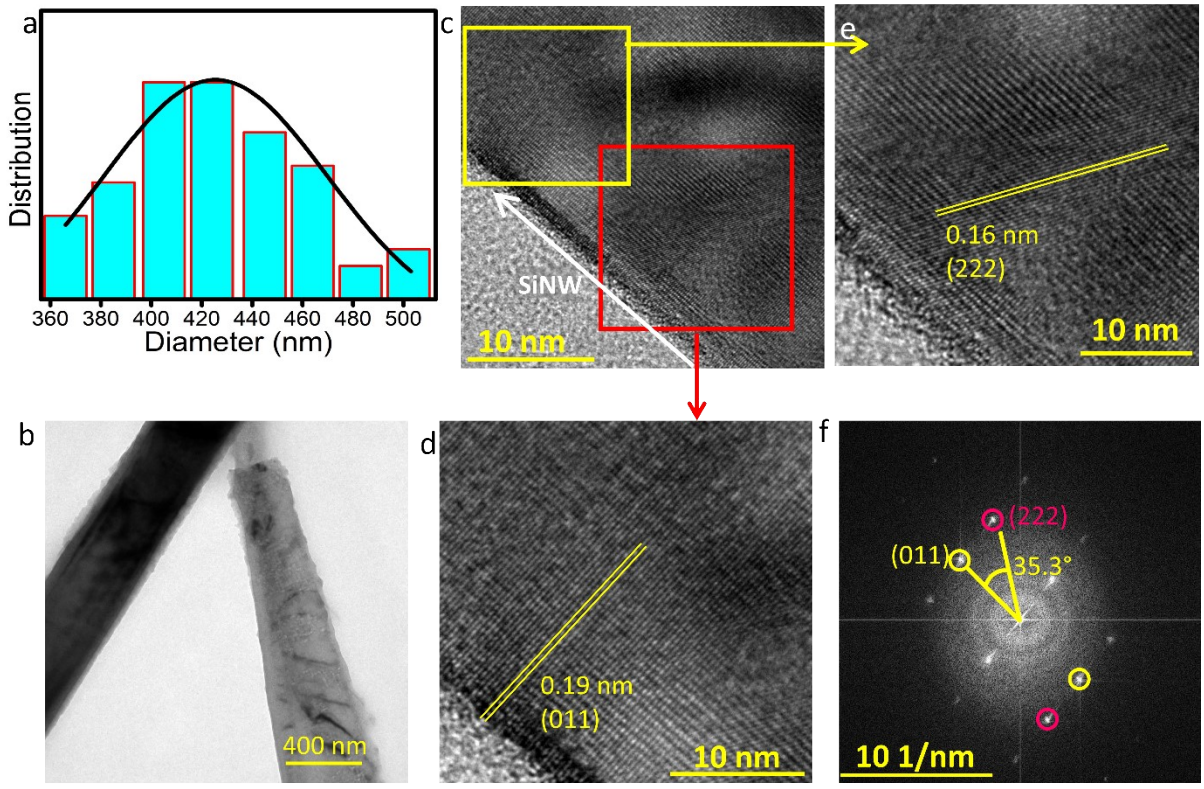

Fig. S2. Morphological analysis of SiNW. (a) SiNW diameter distribution. (b) TEM image of SiNW having a uniform cross-section. (c) HRTEM image showing the lattice fringes for Si, (d) zoomed yellow marked region of Fig. S2c and (e) zoomed red marked region of Fig. S2c, (f) FFT pattern of Fig. S2c.

Supporting Material Note 2: Fig. S2a demonstrates the diameter distribution of SiNWs, and the average diameter is 426 nm. Fig. S2b exhibits the TEM image of SiNW with a diameter of 414 nm, consistent with the average diameter obtained from the SEM image. From the HRTEM image of SiNW Fig. S2c, the high crystallinity of nanowire is comprehensible, which matches well with the X-ray diffraction (XRD) spectra in Fig. S3a. The lattice fringes for Si(011) plane are distinctly visible (Fig. S2d) with a lattice spacing of 0.19 nm, which corroborates the nanowire formation in the [011] direction. The lattice fringes for Si(222) plane are clearly visible with a lattice spacing of 0.16 nm in Fig. S2e which is expected since the nanowire is etched in the Si(111) plane. Bright points in the Fast Fourier transform (FFT) (Fig. S2f) manifest the corresponding (011) plane and (222) plane along with the angle between them which matches well with the theoretical value.

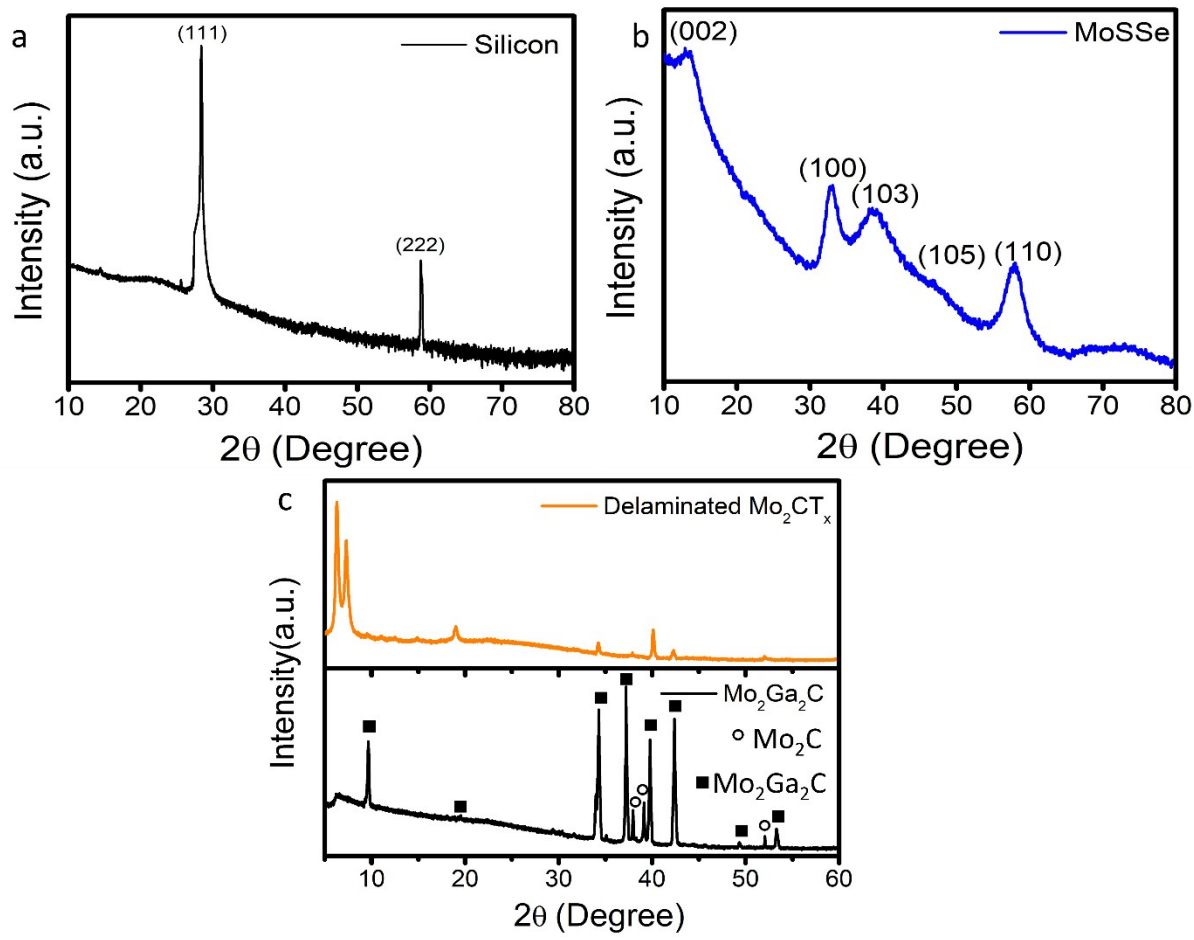

Fig. S3. X-ray diffractogram of (a) SiNW (b) MoSSe and (c) Mo_2CT_x Mxene and its MAX phase Mo_2Ga_2C.

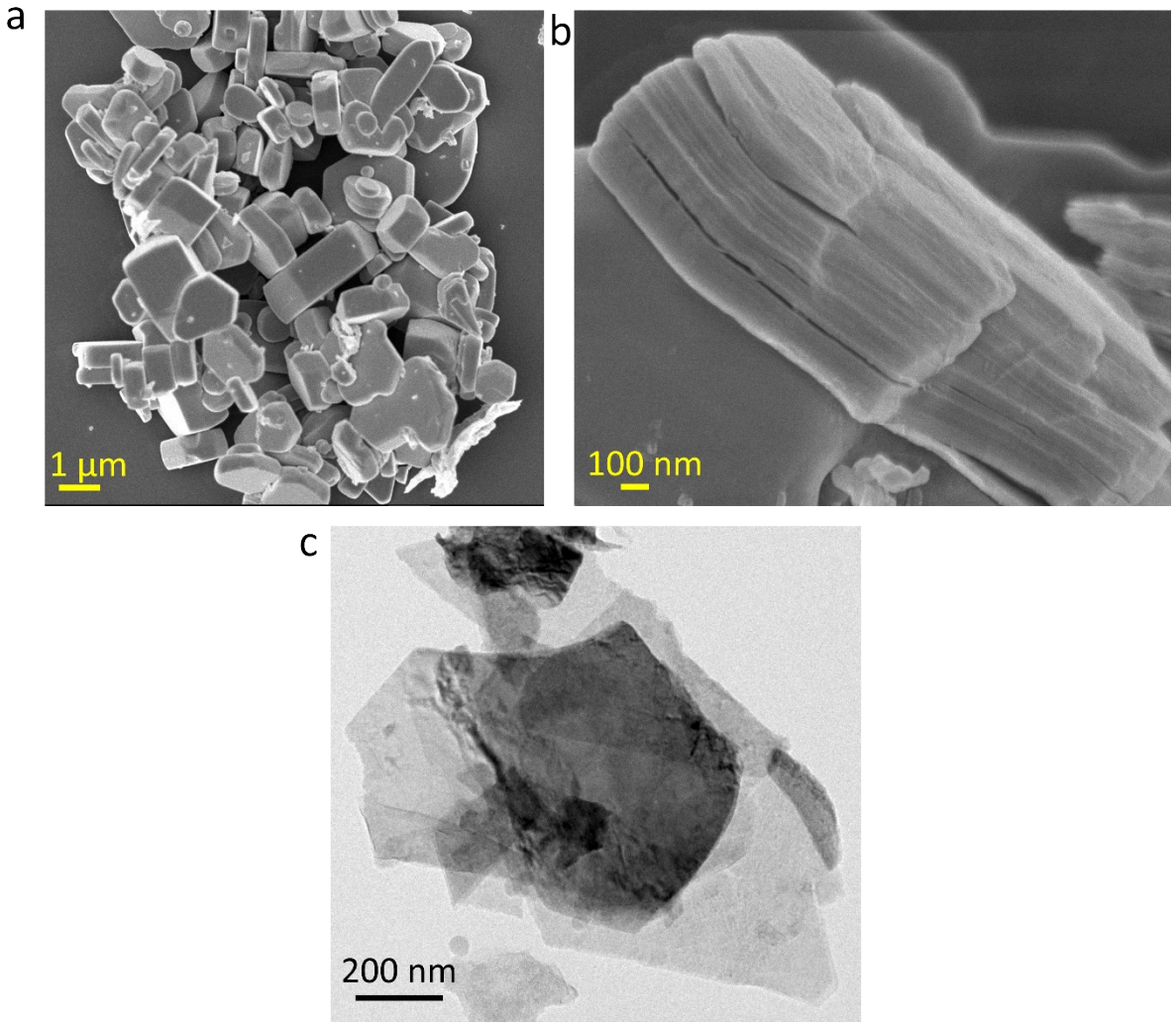

Fig. S4. Morphological characterization of Mo_2Ga_2C MAX and Mo_2CT_x MXene. (a) SEM of Mo_2Ga_2C MAX phase powder and (b) Mo_2CT_x non-delaminated Mxene. (c) TEM image of delaminated Mo_2CT_x Mxene.

Supporting Material Note 3: To understand the overall morphology of the synthesized Mo_2Ga_2C MAX phase and Mo_2CT_x MXene (without and with delamination), we have performed the following characterization. Fig. S4a is showing the morphology of Mo_2Ga_2C MAX phase. After etching of MAX phase, the quintessential layered structure of Mo_2CT_x MXene is revealed by the SEM image (Fig. S4b). Fig. S4c shows Mo_2CT_x MXene in its delaminated form with few-layer thickness.

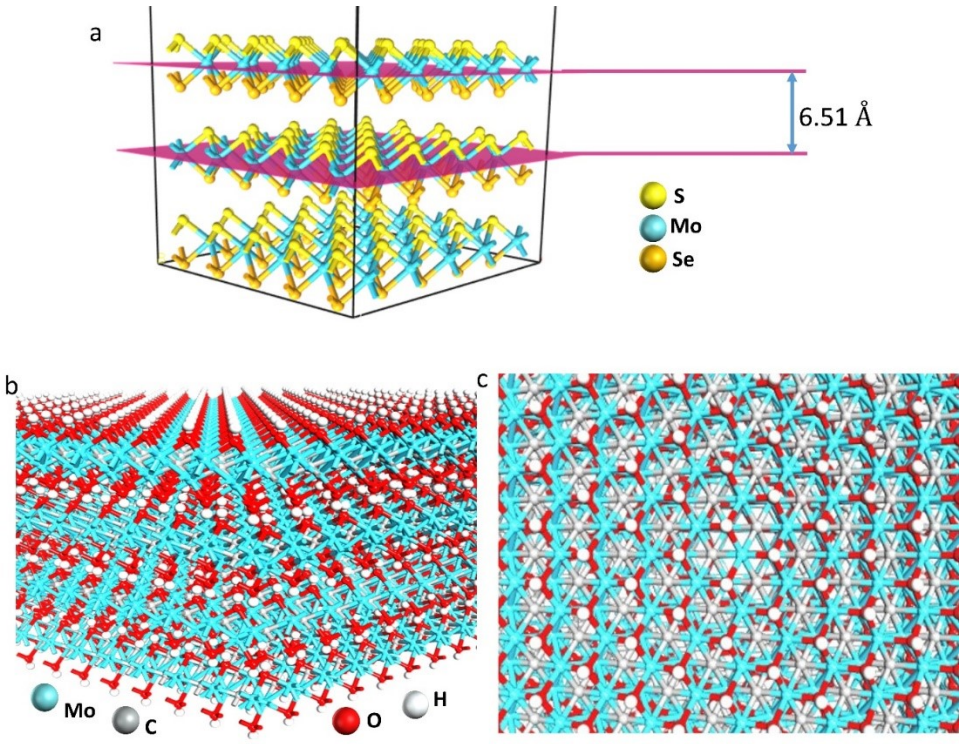

Fig. S5. Atomic structure illustration of (a) 3-layer MoSSe indicating interlayer distance. (b) Mo_2C MXene with the functional group (-OH) with side and (c) top view. The representative atomic colours of Mo, C, O, and H are given.

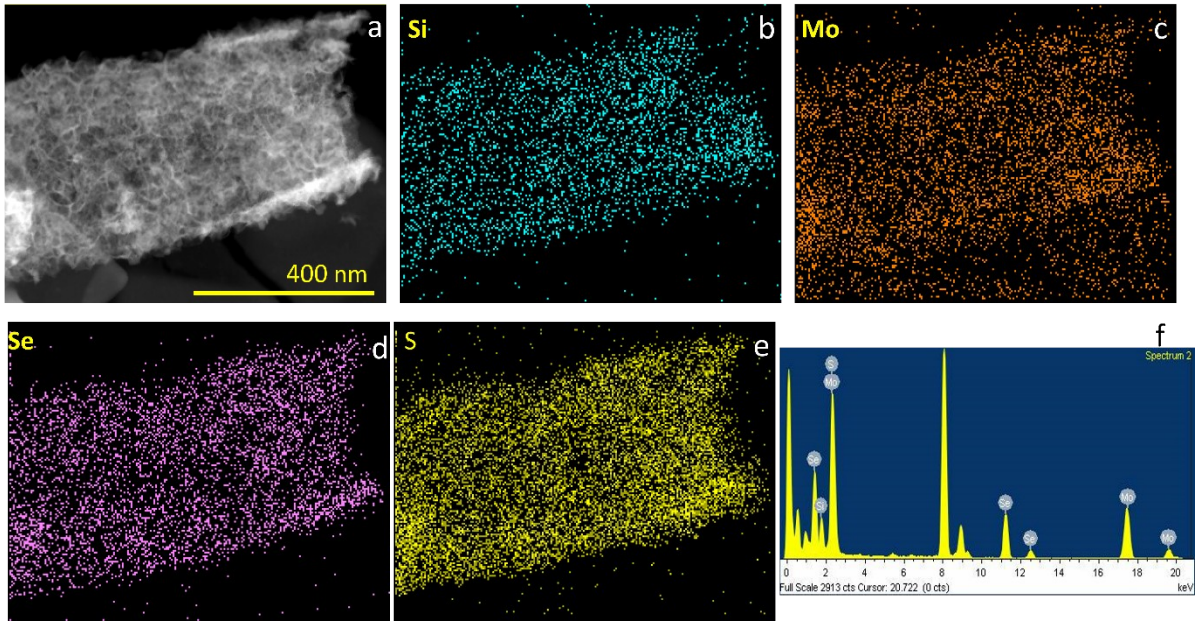

Fig. S6. Elemental analysis. (a) HAADF-STEM image of Mo_2CT_x/MoSSe/SiNW and corresponding mapping of (b) Si, (c) Mo, (d) Se and (e) S. (f) Associated EDX spectra.

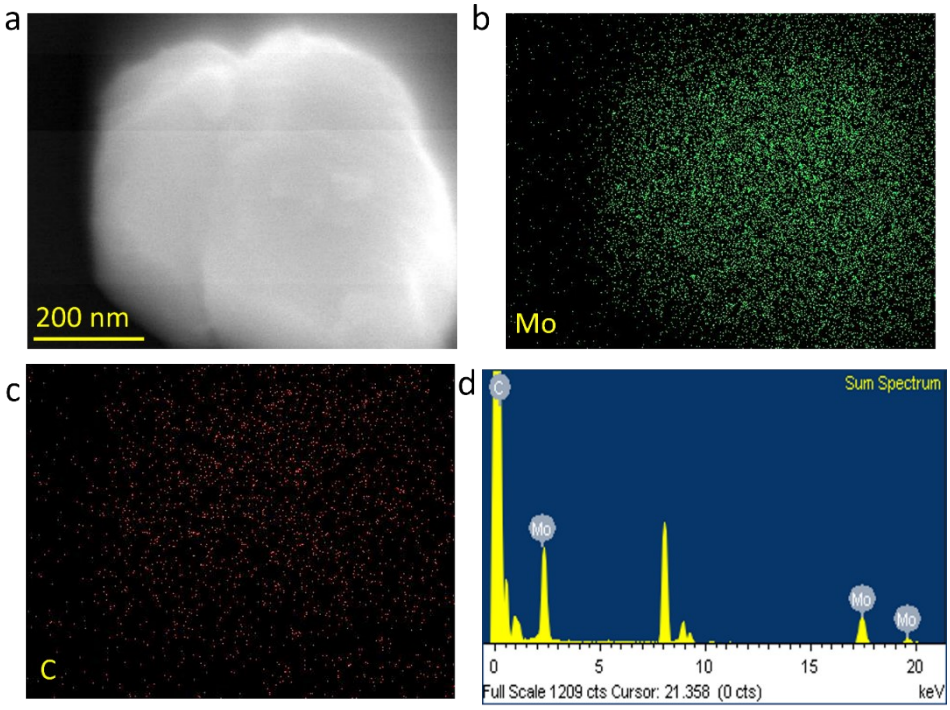

Fig. S7. SEM-EDS mapping of Mo_2CT_x Mxene. (a) Associated image and mapping of (b) Mo, (c) C, and (d) corresponding EDX spectra.

Supporting Material Note 4: Detailed elemental analyses are carried out to understand the elementwise distribution of MoSSe and Mo_2CTx. HAADF-STEM image of MoSSe grown SiNW decorated with Mo_2C-T_x is shown in Fig. S6a, and the corresponding elemental maps of Si (16.86 atomic %), Mo (45.60 atomic %), Se (18.22 atomic %), S (19.33 atomic %) are shown in Fig. S6b,c,d,e respectively, that corroborates uniform and homogenous distribution of the constituents. The associated energy-dispersive X-ray spectroscopy (EDX) data is displayed in Fig. S6f. SEM-EDX analysis of Mo_2C shows SEM image (Fig. S7a) and corresponding mapping of elemental Mo (63.33 atomic %) and C (36.67 atomic %) (Fig. S7b,c respectively), which elucidates uniform distribution of Mo and C and no presence of Ga, i.e., it is successfully etched out (EDX spectra is shown in Fig. S7d).

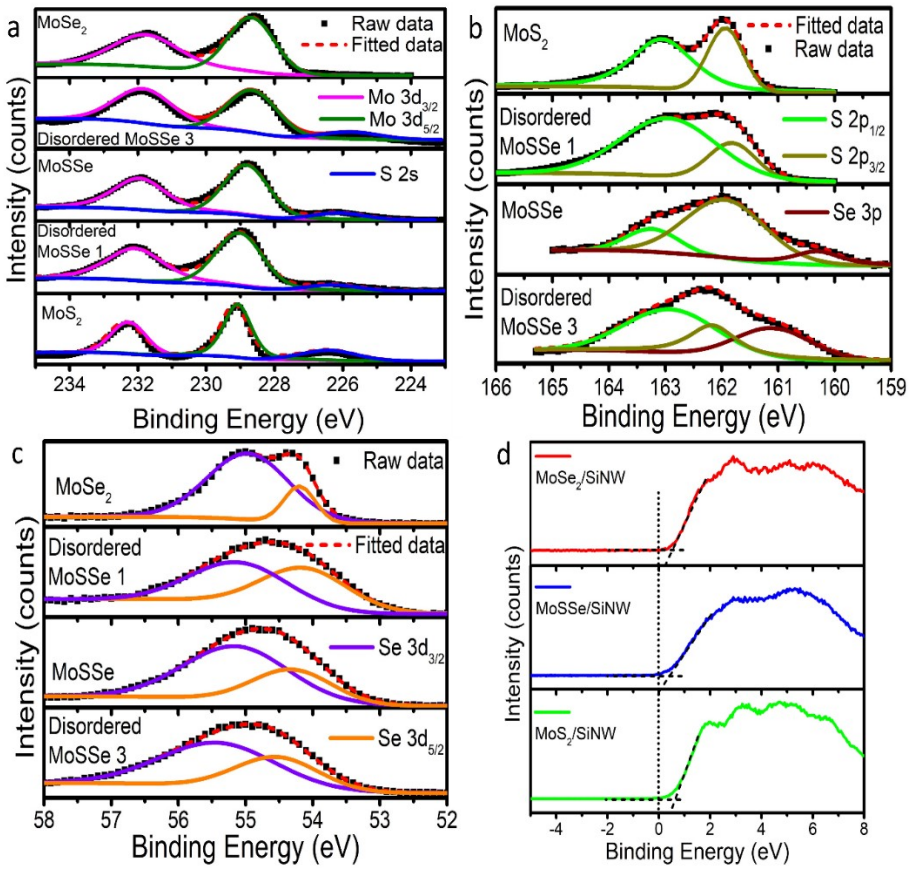

Fig. S8. XPS spectra for (a) Mo 3d, (b) S 2p and (c) Se 3d of $MoSe_2$/Si, MoSSe 1/Si, MoSSe 3/Si, MoSSe/Si and MoS_2/Si as mentioned above in the plot. (d) Valence band spectra of different photocathodes.

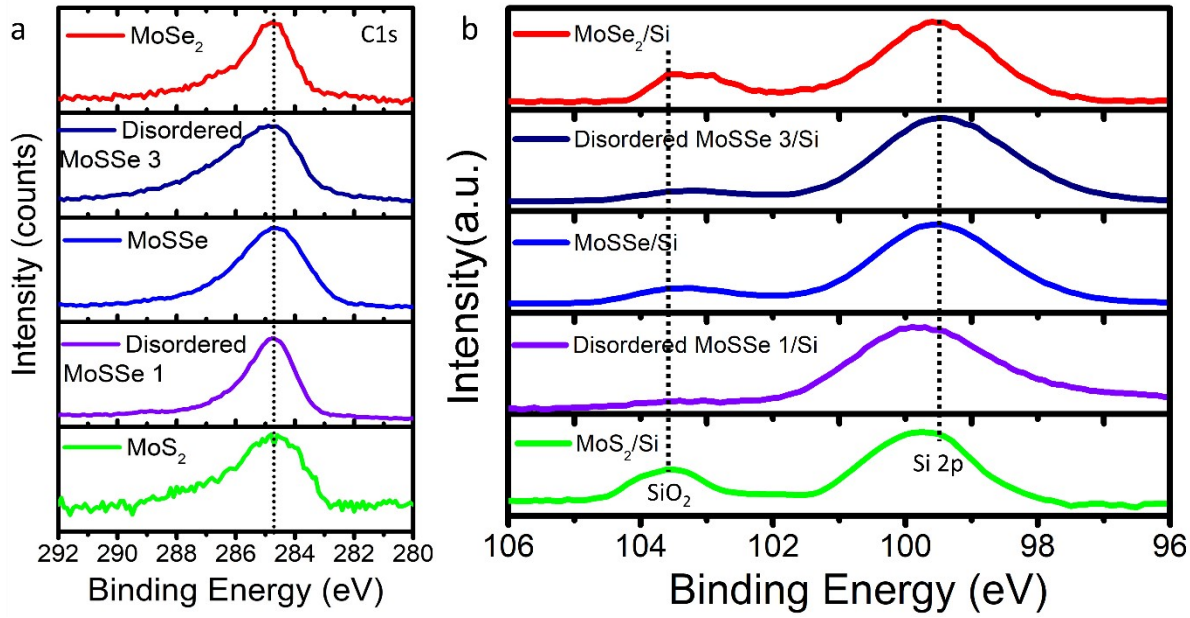

Fig. S9. (a) XPS spectra for C1s peak correction and (b) Si 2p.

Supporting Material Note 5: To investigate the chemical states of molybdenum and chalcogen (S, Se), XPS analysis has been carried out. Distinguishing various oxidation states or elements helps to identify the systematic evolution from symmetrical MX_2 (MoS_2, $MoSe_2$) to asymmetrical MXY (MoSSe). For the sake of clarity, C1s peaks were corrected to 284.4eV for all the samples (Fig. S9a). The high-resolution narrow spectrum for Mo ($3d_{5/2}$ and $3d_{3/2}$) is located in the binding energy range 228−232eV, which is characteristic of the Mo^{+4} oxidation state (Fig. S8a). Now, if we start from MoS_2 having Mo $3d_{5/2}$ peak at ~229.10 eV and $Mo3d_{3/2}$ peak at ~ 232.62 eV, we can observe a gradual shift of both $Mo3d_{5/2}$ and $Mo3d_{3/2}$ peaks to lower binding energy as Se is added systematically in the MoS_2 matrix. The shift in binding energy could be attributed to the difference in electronegativity between Se and S atoms, indicating a slight change in the oxidation state of Mo. Interestingly, the spin-orbit splitting energy (ΔE) ~3.14 eV typical for Mo^{+4} oxidation state is best suited for the Janus MoSSe. Along with the Mo 3d peak, a small peak for S2s peak is also visible except for $MoSe_2$. The deconvoluted XPS peaks of S 2p provide prominent $S2p_{1/2}$ and $2p_{3/2}$ peaks (Fig. S8b) for MoS_2 and disordered MoSSe 1, whereas additional peaks correspond to Se 3p could be observed starting from Janus MoSSe. In the case of disordered MoSSe 3, the Se 3p peak is more dominating than the intensity ratio $S2p_{1/2}/2p_{3/2}$ has been altered, signifying a disordered structure. The Se3d peak is (Fig. S8c) also deconvoluted to $Se3d_{5/2}$ and $Se3d_{3/2}$ in the binding energy range 57.5−52.4 eV.

From the XPS spectra of Si 2p of the heterostructure over SiNW, Si-Si bonding is found as obvious and also the signature of little SiO_2 (Fig. S9b) is found. The main origin of SiO_2 is due to nanowire formation. The valance band spectra (Fig. S8d) indicated higher valence band maxima (VBM) position with respect to Fermi level (E_f) for MoS_2/SiNW (0.51 eV) and $MoSe_2$/SiNW (0.56 eV) compared to MoSSe/SiNW (0.43 eV). Smaller VBM position *w.r.t* E_f

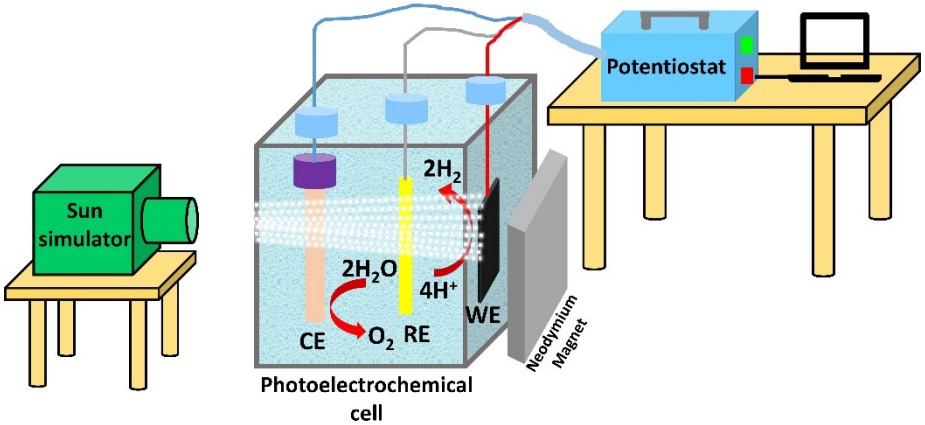

Fig. S10. Schematic representation of PEC cell, sun simulator and external magnet.

facilitates electron flow due to lower band bending. Also, the VBM position *w.r.t* E_f indicated a perfect p-type nature ideal for water reduction.

Supporting Material Note 6: The setup for applying a magnetic field to the photocathode in the photoelectrochemical (PEC) cell, along with the magnet arrangement, is schematically illustrated in Figure S10. A neodymium permanent magnet was positioned in parallel with the backside of the photocathode, just outside the PEC cell, for both photo and dark conditions. The magnetic field strength was varied by adjusting the distance between the magnet and the photocathode or by using magnets with different magnetic strengths. To maintain consistency, the magnet was held in a specific orientation throughout the entire photoelectrochemical measurement. The south pole of the magnet was oriented to face the backside of the photocathode, while the north pole faced outward. Although there was a minimal difference when the arrangement was reversed, with the north pole facing the backside of the photocathode and the south pole outward, the former orientation was selected for all photoelectrochemical measurements. To quantify the strength of the magnetic field, a gauss meter was employed for accurate measurements.

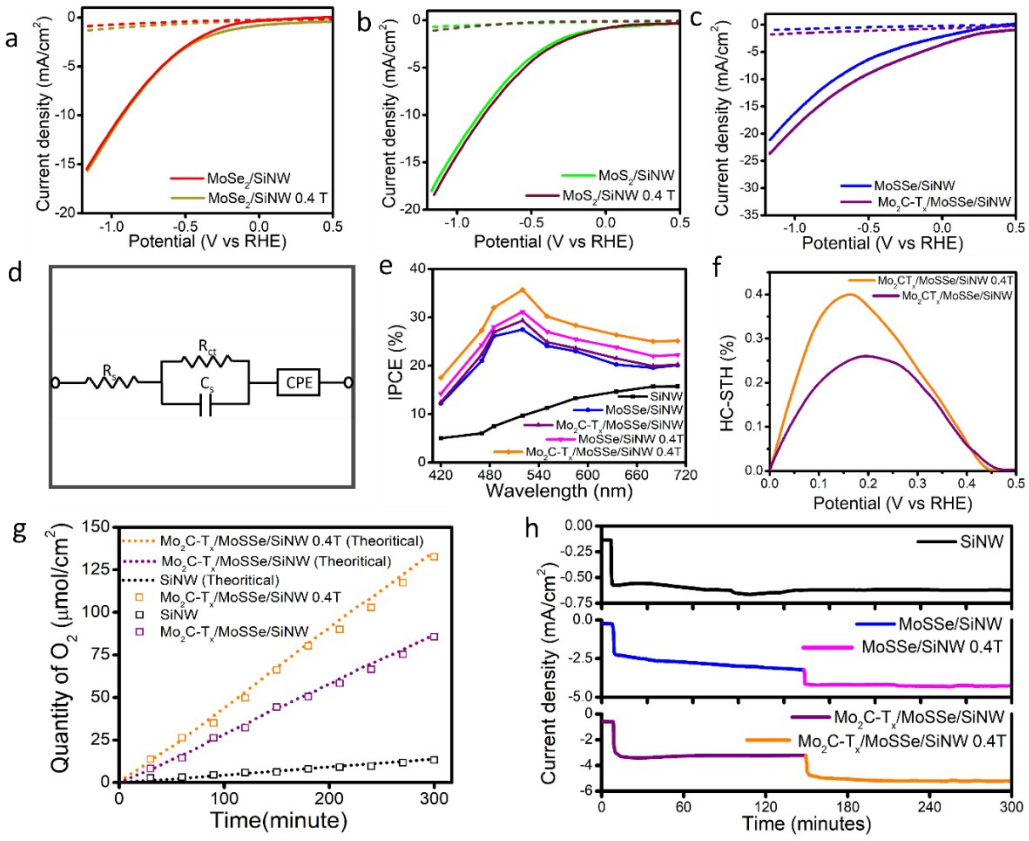

Fig. S11. (a) LSV plot of $MoSe_2$/SiNW PC with and without magnetic field. (b) LSV plot of MoS_2/SiNW PC with and without magnetic field. (c) LSV plot to compare between

MoSSe/SiNW PC and Mo_2CTx/MoSSe/SiNW PC. (d) EIS fitting circuit. (e) Efficiency calculations for SiNW, MoSSe/SiNW PC and Mo_2CT_x/MoSSe/SiNW PCs (with and without

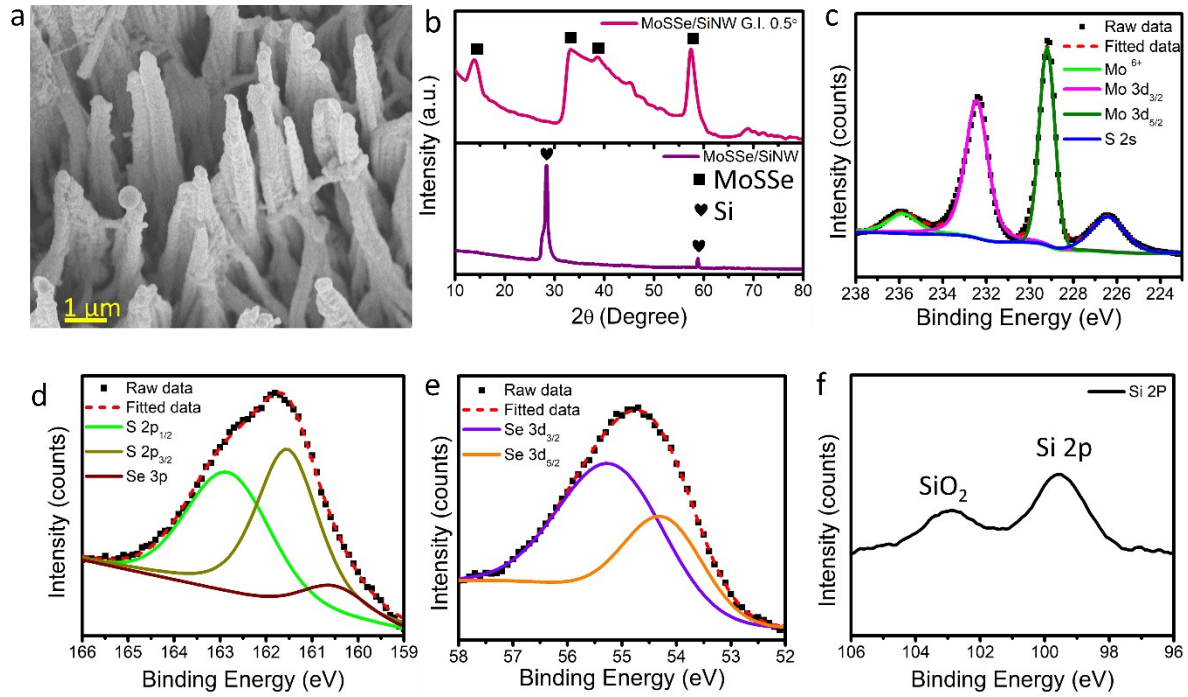

Fig. S12. Characterization for morphology, crystal phase and valence after PEC reaction. (a) SEM image of MoSSe grown SiNWs. (b) Grazing incident angle XRD of MoSSe/SiNW array. XPS spectra for (c) Mo 3d, (d) S 2p, (e) Se 3d and (f) Si 2p.

magnetic field) at various incident light wavelength. (f) HC-STH of Mo_2CT_x/MoSSe/SiNW PC with and without magnetic field. (g) Product O_2 gas quantification. (h) Stability of different PCs with and without magnetic field.

Supporting Material Note 7: Incident photon-to-current efficiency was calculated following the below equation:

$$IPCE = \frac{I_{Ph}(A\ cm^{-2})}{P_{in}(W\ cm^{-2})} \times \frac{1240}{\lambda(nm)} \times 100\%$$

Where I_{ph} is photocurrent density, P_{in} is the input power, λ is the wavelength of incident light.

HC-STH efficiency was calculated following the below equation:

$$HC-STH = \frac{|(j_p - j_d)| \times (E_{RHE} - E_{H^+/H_2}) \times 100}{P_{in}} \%$$

Where j_p and j_d is the current density under photo illumination and dark respectively at E_{RHE}, $E_{H+/H2}$ is 0 V_{RHE}, P_{in} is the input power of the AM 1.5 solar spectrum.

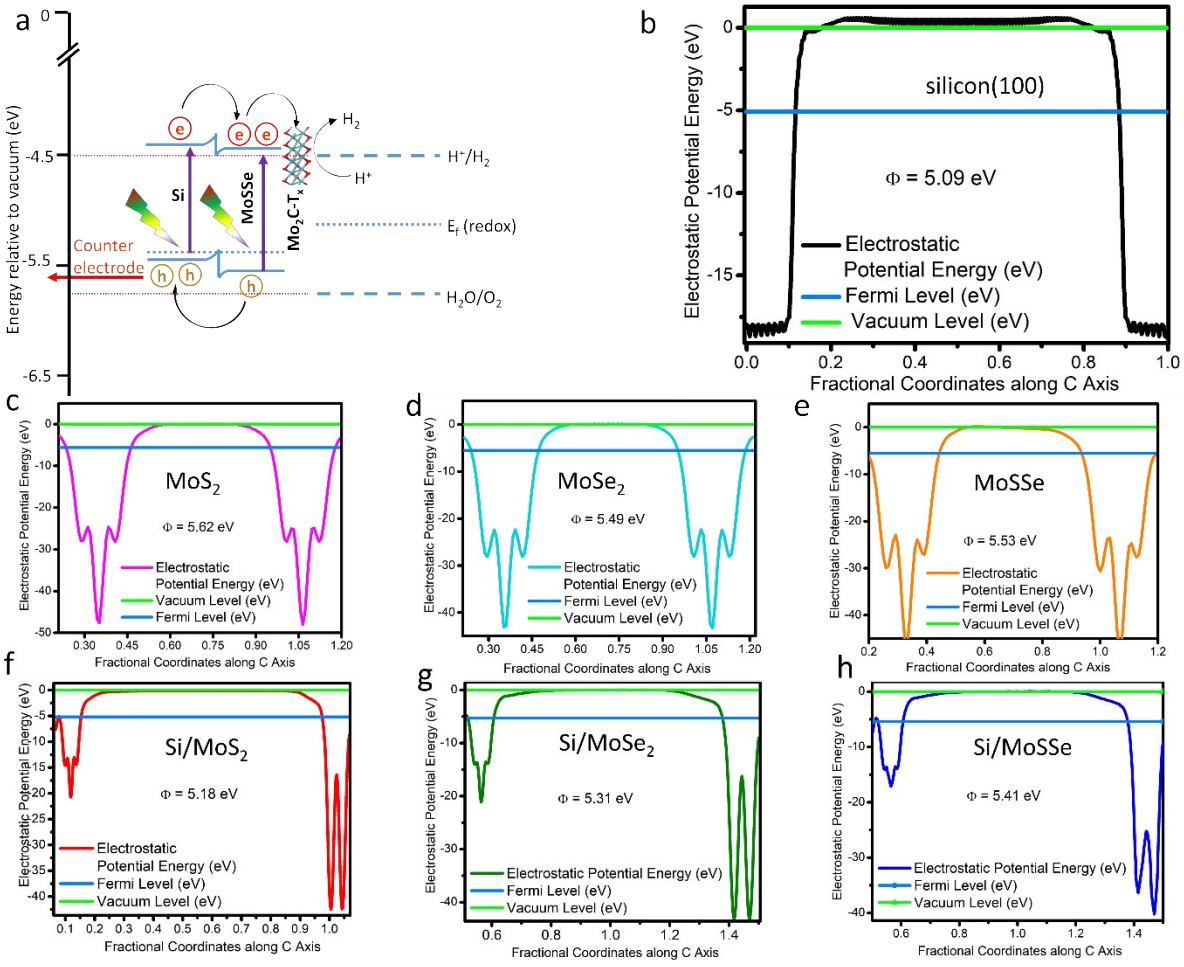

Fig. S13. (a) Energy band alignment of Mo_2CT_x/MoSSe/SiNW PC. Electrostatic potential energy profile of (b) silicon (100), (c) MoS_2, (d) $MoSe_2$, (e) MoSSe, (f) Si(100)/MoS_2, (g) Si(100)/$MoSe_2$, (h) Si(100)/MoSSe.

Supporting Material Note 8: The energy band diagram of Mo_2CT_x/MoSSe/SiNW PC is shown in Fig. S13a. The excited photo carriers from silicon move towards MoSSe. The excited photocarrier of MoSSe along with those electrons received from Si efficiently channelled to water (electrolyte) through Mo_2CT_x Mxene having high metallic conductivity. On the other hand, holes from MoSSe move towards Si and finally in the direction of a counter electrode *via* an external circuit. In order to propose the energy band alignment, we have calculated the electrostatic potential energy profile of pristine materials and their heterostructures as well. The work function of different materials and their heterostructure are found to be 5.09 eV, 5.62 eV, 5.49 eV, 5.53 eV, 5.18 eV, 5.31 eV and 5.41 eV for silicon (100) (Fig. S13b), MoS_2 (Fig. S13c), $MoSe_2$ (Fig. S13d), MoSSe (Fig. S13e), Si(100)/MoS_2 (Fig. S13f), Si(100)/$MoSe_2$ (Fig. S13g) and Si(100)/MoSSe (Fig. S13h), respectively.

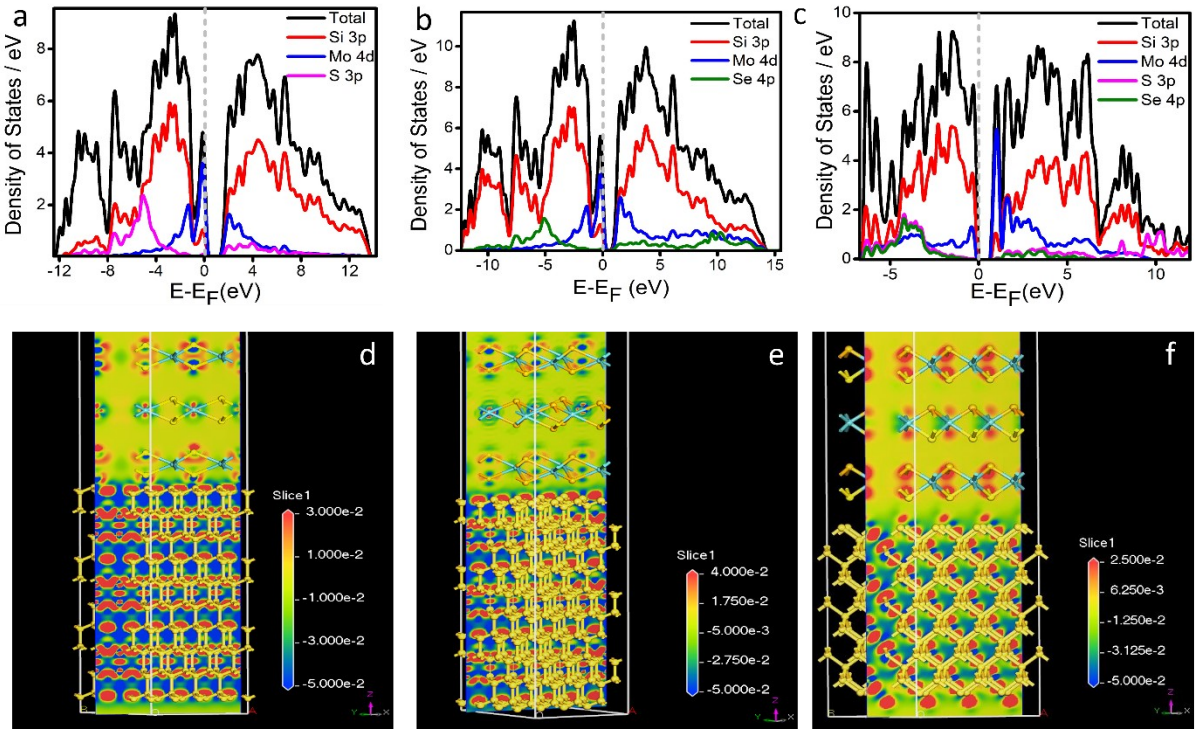

Fig. S14. PDOs plot of (a) MoS_2/Si, (b) $MoSe_2$/Si, (c) MoSSe/Si. EDD slice of (d) MoS_2/Si, (e) $MoSe_2$/Si and (f) MoSSe/Si(100)

Supporting Material Note 9: PDOS and EDD simulations have been carried out to understand hybridization at the interface and charge transfer between the two layers. From the PDOS plots of MoS_2/Si (Fig. S14a) and $MoSe_2$/Si (Fig. S14b), it can be observed that both the VBM and conduction band minima (CBM) have a significant contribution from the Mo 4d orbitals indicating that the band edges in the heterostructure are dominated by MoS_2 and $MoSe_2$ respectively. In both MoS_2 and $MoSe_2$, the valence band (VB) shows an overlap between the

Si 3p and Mo 4d orbitals indicating a Si-Mo 3p-4d hybridization acting as a charge transfer pathway between the two layers. In addition to that, an overlap between the Si 3p-S 3p and Si 3p-Se 4p for MoS_2 and $MoSe_2$, respectively have been observed, indicating a significant degree of hybridization between the Se and S atoms with Si at the interface, since the MoS_2 and $MoSe_2$ are connected to the Si surface via the S and Se atoms respectively. However, the extent of overlap between the Se 4p and Si 3p is lower compared to S 3p and Si 3p due to the higher energy gap between the 3p and 4p orbitals resulting in poor hybridization compared to S 3p whose energy level is closer to Si 3p. In MoSSe/Si, an additional hybridization between the S and Se atoms (Fig. S14c) has been observed as expected for Janus materials. Mulliken population analysis along with EDD plots have been carried out for analyses of charge transfer pathways in the heterostructure. A charge of -0.21|e| was transferred from Si to MoS_2 for Fermi level equilibration since the work function of MoS_2 is higher than Si. From the EDD plot (Fig. S14d), an electron density enrichment over the S atoms in the MoS_2 layer has been observed simultaneously with an electron density depletion over the Si atoms at the interface indicated by the blue color of the EDD plot at the interface. Hybridization of $MoSe_2$ with Si was observed to be relatively poor with a charge transfer of -0.14|e| from the Si to Se atoms (Fig. S14e). In both cases, it was observed that the lowermost layer was the most active participant in charge transfer and hybridization while the upper layers remained unchanged in electron density. A very high charge transfer of -0.27 |e| and -0.29|e| was observed for MoSSe/Si(111) and MoSSe/Si(100) (Fig.S14f), which is most likely due to the presence of an additional S-Se hybridization pathway.

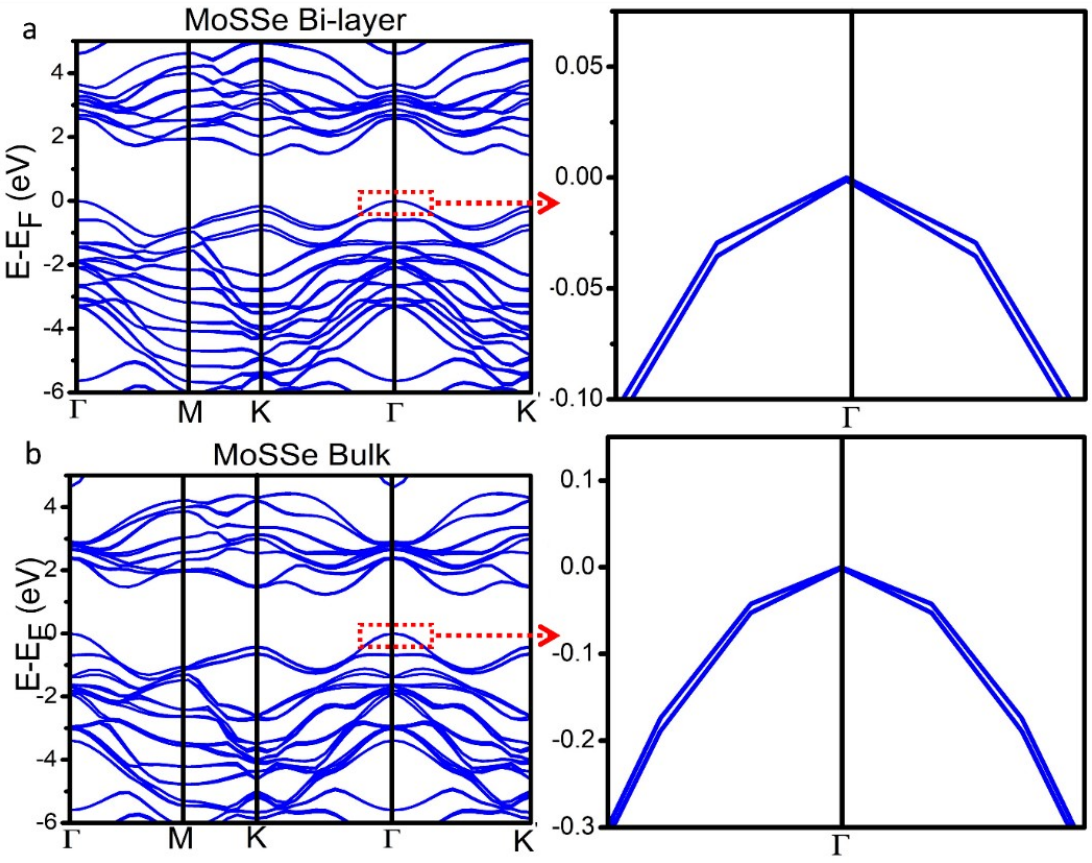

Fig. S15. (a) Band structure of bi-layer MoSSe, zoomed red marked region at right showing Rashba splitting at Γ point. (b) Band structure of bulk MoSSe, zoomed red marked region at right showing Rashba splitting at Γ point.

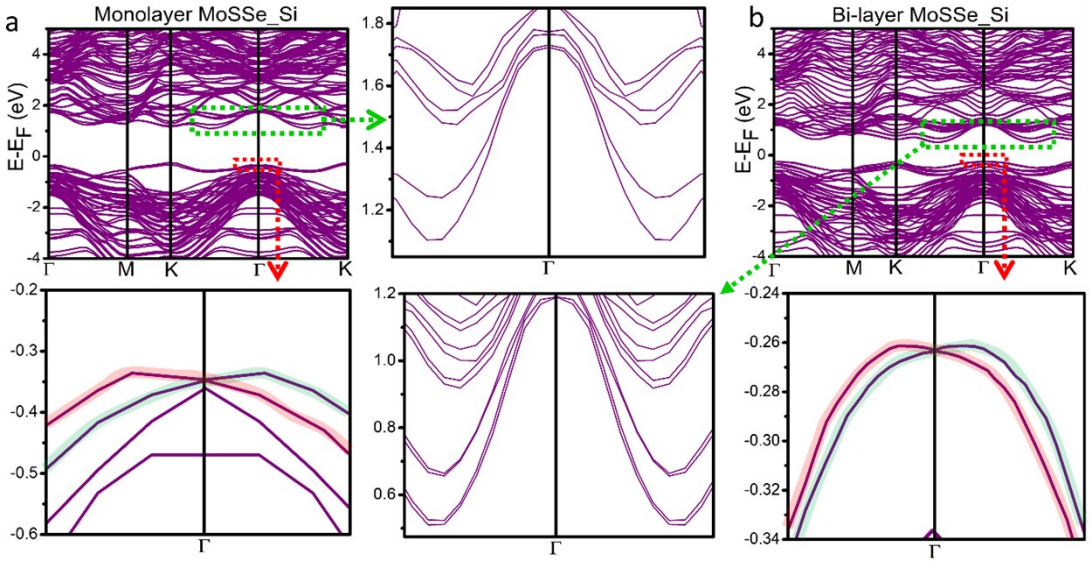

Fig. S16. (a) Band structure of monolayer MoSSe/Si, zoomed green marked region at the right side, shows Zeeman splitting at Q/Q′ point and zoomed red marked region is showing Rashba splitting below. (b) Band structure of bi-layer MoSSe/Si, zoomed green marked region at

diagonally left shows Zeeman splitting at Q/Q′ point and zoomed red marked region is showing Rashba splitting below.

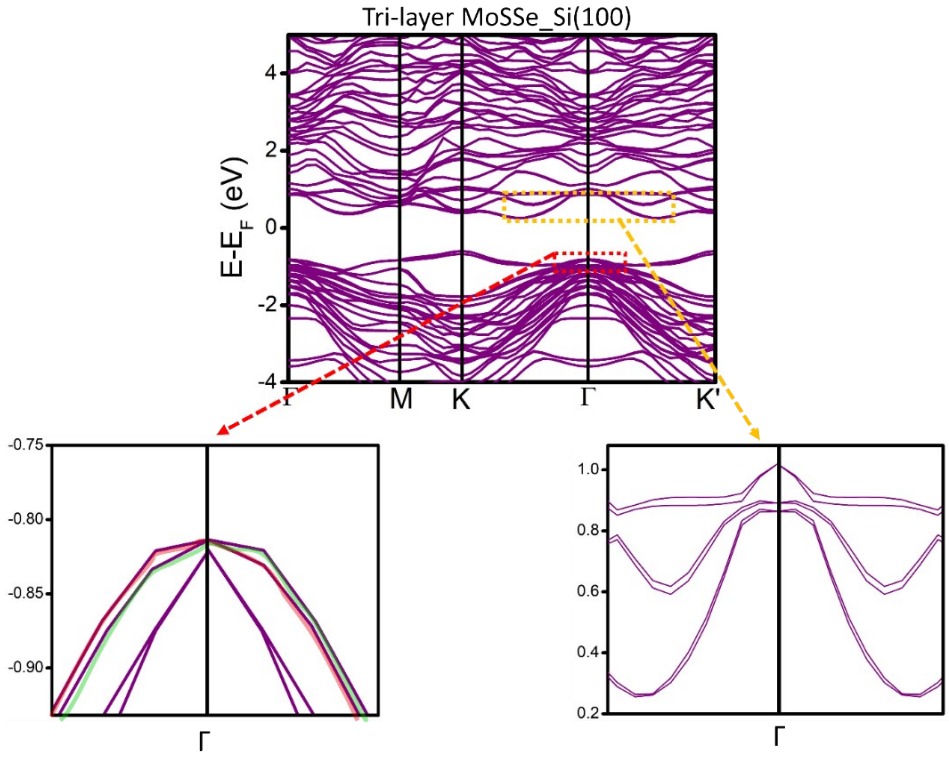

Fig. S17. Band structure of trilayer MoSSe/Si(100), zoomed yellow marked region at the right side, shows Zeeman splitting at Q/Q′ point and zoomed red marked region is showing Rashba splitting below.

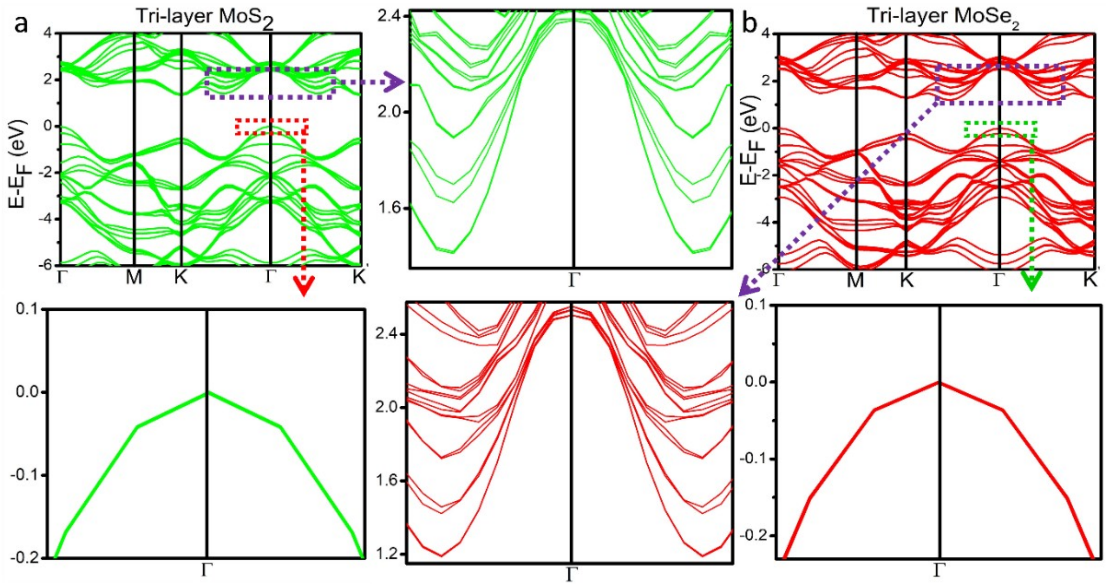

Fig. S18. (a) Band structure of tri-layer MoS_2, zoomed violet marked region at the right side shows insignificant Zeeman splitting at Q/Q′ point and zoomed red marked region is showing no Rashba splitting below. (b) Band structure of tri-layer $MoSe_2$, zoomed violet marked region

at diagonally left shows insignificant Zeeman splitting at Q/Q′ point and zoomed green marked region is showing no Rashba splitting below.

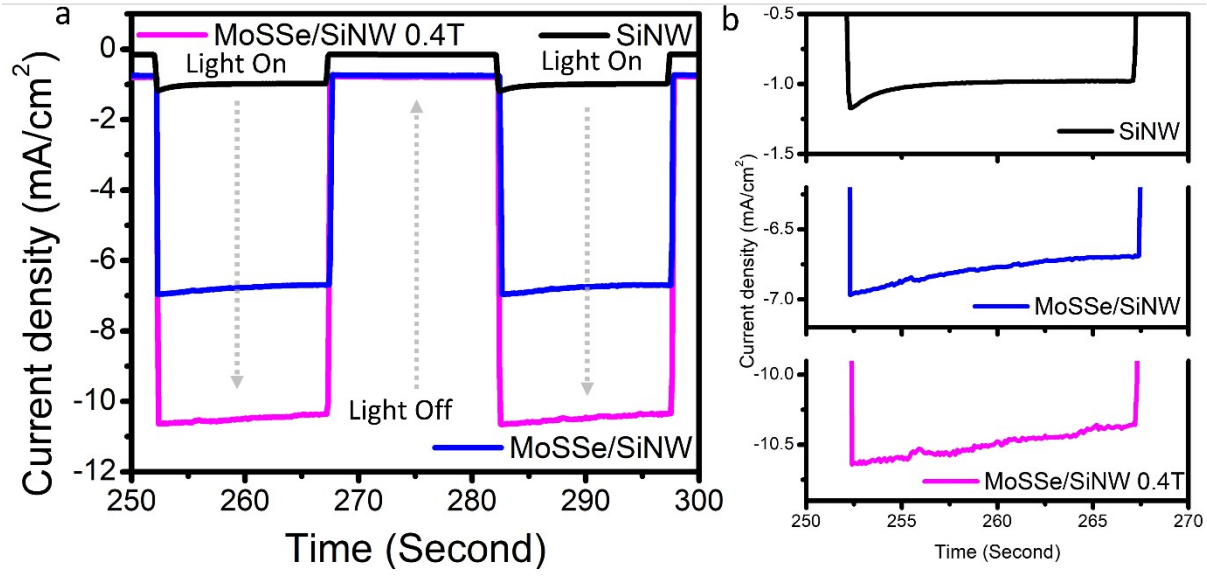

Fig.S19. (a) Photo response through chronoamperometry under chopped illumination. (b) Zoomed region of 15 second light on period of Fig. S19a.

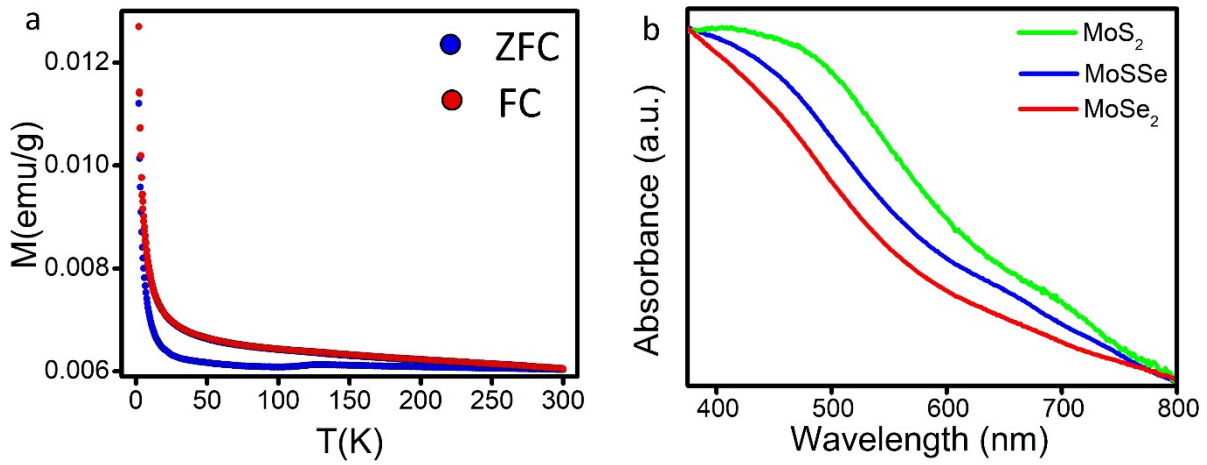

Fig. S20. (a) ZFC-FC plot of MoSSe. (b) UV-Vis-NIR absorption spectra of MoS_2, MoSSe and $MoSe_2$

Supporting Material Note 10: No Rashba spin splitting is observed in few-layer MoS_2 (Fig. S18a, zoomed red marked region) and $MoSe_2$ (Fig. S18b, zoomed green marked region) . Zeeman splitting at CBM is also negligible for MoS_2 (Fig. S18a, zoomed violet marked region) and $MoSe_2$ (Fig. S18b, zoomed violet marked region). It is already discussed that $MoSe_2$ shows entirely DM behaviour through MoS_2 shows FM character with a low moment at the lower external magnetic field. Due to the absence of all these crucial parameters, magnetic

enhancement of photocurrent is not attainable for MoS_2 and $MoSe_2$. Little enhancement of photocurrent in the LSV plot of MoS_2 (Fig. S11b) and $MoSe_2$ (Fig. S11a) can be attributed as magneto-hydrodynamic flow.

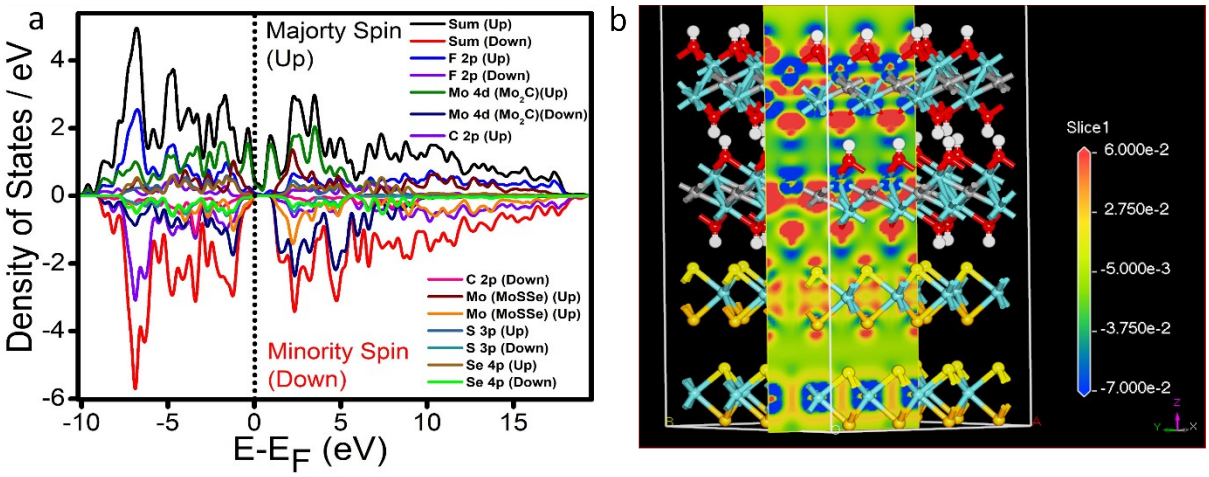

Fig. S21. (a) PDOS plot for Mo_2CT_x/MoSSe. (b) EDD slice for Mo_2CT_x/MoSSe.

Supporting Material Note 11: PDOS plot (Fig. S21a) for Mo_2CT_x/MoSSe shows a strong degree of overlap with the Mo atoms in the MoSSe layer and the Mo atoms in the Mo_2CT_x layer, indicating a strong Mo-Mo 4d interaction acting as a charge transfer pathway between the two layers. MXene acts as a strong electrocatalyst for reducing overpotential and reducing photo-generated carrier recombination by facilitating rapid charge separation[13]. Thus, a strong degree of overlap increased DOS at the Fermi level, and a low bandgap is important for the heterostructure. For MoSSe, a negligible bandgap for the spin-polarized α DOS is observed while a bandgap for the β states is observed, indicating a semi-metal-like nature of the heterostructure, which provides the crucial enhancement in electronic conductivity essential for charge separation. The OH functional groups also play a very important role at the interface as observed from the EDD plot (Fig. S21b), a significant interaction between the H atoms of the OH groups and S/Se atoms in the Se layer can be seen. In Mo_2CT_x/MoSSe, an increase in DOS peak width and increment in DOS value indicates strong hybridization at the interface and improved charge mobility. The EDD plots show significant enrichment of electron density over the S and Se atoms in MoSSe along with a depletion around the functional groups in the Mo_2C layer, indicating a high degree of charge transfer between the two layers from Mo_2C to MoSSe.

References:

1 W. Niu, T. Moehl, P. Adams, X. Zhang, R. Lefèvre, A. M. Cruz, P. Zeng, K. Kunze, W. Yang and S. D. Tilley, *Energy Environ. Sci.*, 2022, 2002–2010.

2 S. Gopalakrishnan, G. Paulraj, M. K. Eswaran, A. Ray, N. Singh and K. Jeganathan, *Chemosphere*, 2022, **302**, 134708.

3 M. Kumar, B. Meena, P. Subramanyam, G. Ummethala, S. R. K. Malladi, S. Dutta-Gupta and C. Subrahmanyam, *Energy and Fuels*, 2023, **37**, 2340–2349.

4 W. Yang, J. H. Kim, O. S. Hutter, L. J. Phillips, J. Tan, J. Park, H. Lee, J. D. Major, J. S. Lee and J. Moon, *Nat. Commun.*, 2020, **11**, 861.

5 H. Lin, S. Li, G. Yang, K. Zhang, D. Tang, Y. Su, Y. Li, S. Luo, K. Chang and J. Ye, *Adv. Funct. Mater.*, 2020, **2007071**, 1–9.

6 S. Gopalakrishnan, M. R. Sahoo, A. Ray, N. Singh, S. Harish, E. S. Kumar and M. Navaneethan, *Sustain. Energy Fuels*, 2023, **7**, 1687–1697.

7 F. Lin, R. Tian, P. Dong, G. Jiang, F. He, S. Wang, R. Fu, C. Zhao, Y. Y. Gu and S. Wang, *J. Colloid Interface Sci.*, 2023, **631**, 133–142.

8 M. Wang, S. Wang, Q. Zhang, S. Pan, Y. Zhao and X. Zhang, *Sol. RRL*, 2022, **6**, 2100798.

9 I. H. Kwak, I. S. Kwon, J. H. Lee, Y. R. Lim and J. Park, *J. Mater. Chem. C*, 2021, **9**, 101–109.

10 K. Roy, S. Maitra, D. Ghosh, P. Kumar and P. Devi, *Chem. Eng. J.*, 2022, 435.

11 L. Hu, J. Wang, H. Wang, Y. Zhang and J. Han, , DOI:10.1021/acsami.2c22423.

12 R. Ghosh, B. Papnai, Y. S. Chen, K. Yadav, R. Sankar, Y. P. Hsieh, M. Hofmann and Y. F. Chen, *Adv. Mater.*, 2023, **35**, 1–7.

13 K. R. G. Lim, A. D. Handoko, L. R. Johnson, X. Meng, M. Lin, G. S. Subramanian, B. Anasori, Y. Gogotsi, A. Vojvodic and Z. W. Seh, *ACS Nano*, 2020, **14**, 16140–16155.